Synergetic Enhancement of Fluorescence and Magnetic Resonance Signals Assisted by Albumin Cage

Lirong Wang,[1] Qing Wan,[1] Rongyuan Zhang,[6] Bo Situ,[3] Kaiyuan Ni,[5] Jinhao Gao,[2] Zhiming Wang,[1], Anjun Qin,[1],* Ben Zhong Tang[1,4]*

Dr. L. Wang, Dr. Q. Wan, Prof. Z. Wang, Prof. A. Qin, Prof. B. Z. Tang
State Key Laboratory of Luminescent Materials and Devices, Guangdong Provincial Key Laboratory of Luminescence from Molecular Aggregates, SCUT-HKUST Joint Research Institute, AIE Institute, Center for Aggregation-Induced Emission, South China University of Technology (SCUT), Guangzhou 510640, China.
E-mail: wangzhiming@scut.edu.cn, msqinaj@scut.edu.cn
Prof. B. Z. Tang
Department of Chemistry, Hong Kong Branch of Chinese National Engineering Research Center for Tissue Restoration and Reconstruction, Institute for Advanced Study, and Department of Chemical and Biological Engineering, The Hong Kong University of Science and Technology, Clear Water Bay, Kowloon, Hong Kong, China.
Prof. J. Gao
Department of Chemical Biology, College of Chemistry and Chemical Engineering, Xiamen University, Xiamen 361005, China.
Dr. B. Situ
Department of Laboratory Medicine, Nanfang Hospital, Southern Medical University, Guangzhou 510515, China.
Dr. K. Ni
Koch Institute for Integrative Cancer Research, Massachusetts Institute of Technology, Cambridge, MA, USA.
Dr. R. Zhang
Department of Urology, The First Affiliated Hospital of Soochow University, 188 Shizi Road, Suzhou 215006, China.

Keywords: albumin cage, fluorescence, magnetic resonance signal, aggregation-induced emission, synergetic enhancement

Bimodal fluorescence and magnetic resonance imaging (FLI/MRI) is important for early diagnosis of malignant tumors. Yet, facile and opportune strategies to synergistically enhance fluorescence intensity and magnetic resonance (MR) contrast effect have been rarely reported. Here, a facile albumin cage (AC) strategy is provided to synergistically enhance the fluorescence intensity by aggregation-induced emission (AIE) and MR contrast with prolonged rotational correlation time (τ_R) of Gd(III) chelates and diffusion correlation time (τ_D) of surrounding water molecules. The amphiphilic bimodal FLI/MRI probe of NGd, could be facilely loaded into ACs to generate supramolecular structure of NGd-albumin cages (NGd-ACs), which show excellent biocompatibility and biosafety, and exhibit superior fluorescence

1

quantum yield and r_1 over NGd with 6- and 8-fold enhancement, respectively. Moreover, compared with clinical MRI contrast agent of Gd-DOTA, r_1 of NGd-AC shows 17-fold enhancement. As a result, NGd-ACs successfully elicit high-performance bimodal FLI/MRI *in vitro* and brighter MR signals are observed in liver and tumor after intravenous injection of NGd-ACs with a dosage of 6 μmol Gd(III)/kg body weight. This strategy is generic and feasible, and successfully realizes a "1+1>2" effect for dual-modal FLI/MRI.

1. Introduction

Cancer incidence and mortality are rapidly growing and expected to rank as the leading cause of death in the world.[1] In order to fight against cancer, it is particularly urgent and important to develop accurate diagnostic techniques to detect lesions as early as possible. Multimodal imaging plays an important role in early and accurate diagnosis of malignant tumors.[2] Among the widely used imaging techniques, fluorescence imaging (FLI) shows high sensitivity but is limited with tissue-penetration of light for deep-seated tumors. In stark control, magnetic resonance imaging (MRI) stands out by virtue of non-ionization, unlimited tissue-penetration depth, and high spatial resolution, while is hurdled by low sensitivity due to abundant background signal. Integrating FLI and MRI to realize bimodal FLI/MRI can benefit each other, which arouses great interests among researchers to develop novel bimodal FLI/MRI probes.[3]

FLI/MRI bimodal probes can be simply constructed by conjugating/coupling various fluorescent moieties with Gd chelates.[4] For MR contrast, Gd chelates mainly contribute to T_1 contrast effect and their contrast ability can be quantified by the relaxivity (r_1),[5] which is positively associated to rotational correlation time (τ_R) of contrast agents and diffusion correlation time (τ_D) of water molecules around contract agents.[6] Therefore, it is very important to guarantee that Gd chelates contained in the FLI/MRI bimodal probes are able to easily get access to water molecules in the physiological conditions to enhance the contrast

effect, but the fluorescence intensity of FLI/MRI bimodal probe is usually hammered with notorious aggregation-caused quenching (ACQ) effect in physiological conditions. Aggregation-induced emission (AIE) with the mechanism of restriction of intramolecular motion (RIM) is a meaningful strategy to address this problem.[7] Combining Gd chelates with AIE moieties (AIE-Gd) into amphiphilic bimodal probes would not only enhance the fluorescence intensity but also improve the relaxivity with prolonged τ_R.[4a] Unfortunately, due to the strong hydrophobicity of AIE moieties, the Gd chelates are easily embedded inside the tightly packed aggregates, and couldn't easily get access to ambient water. Opposite strategies for constructing Gd chelates on the outside and AIE moiety on the inside need to be precise designed, which is strongly limited by the properties of substrates and preparation process, making them be not universal and practical.[4a,8] Therefore, to satisfy the constraint of intramolecular motion in hydrophilic environment, we proposed that an amphiphilic structure with geometrically confined space would be ideal to load AIE-Gd bimodal probes for this purpose. Thanks to the hydrophobic interaction and steric hindrance, the intramolecular motion of AIE moieties could be restricted to enhance the fluorescence for FLI. Meanwhile, compared with single molecule, the larger size of nanoaggregates with longer τ_R would strongly improve the relaxivity for MRI. Additionally, the geometrically confined structure of these nanoaggregates facilitate water molecules in and out with slow diffusion rate, that is, prolonged τ_D of water molecules, which would further contribute to the improvement of relaxivity (**Scheme 1**).

For the amphiphilic structures, albumin would be the best choice with incomparable advantages, such as biocompatibility and biodegradability.[9] Different albumin-based biomaterials with desired properties have been developed over the past few decades.[10] By virtue of amphiphilic structure, albumin has been widely reported as superb nanocarriers to either improve the relaxivity[6a,11] or enhance the fluorescence intensity based on RIM of AIE moieties.[12] Inspiringly, we design an amphiphilic FLI/MRI dual-modal probe of NGd by

3

combination of AIE moiety and Gd-DOTA, which could closely bind to bovine serum albumin (BSA). And then, we constructed NGd-Albumin Cages (NGd-ACs) through desolvation and glutaraldehyde coupling BSA to load NGd. Compared with NGd, the fluorescence quantum yield and r_1 of NGd-ACs had a more than 6- and 8-fold improvement, respectively, and their r_1 was almost 17-fold higher than that of clinical contrast agent Gd-DOTA. The phantom images had proven that NGd-ACs showed brighter signals than NGd at the same concentration. Moreover, the results of cell phantom imaging and confocal laser scanning microscope (CLSM) verified that NGd-ACs could be internalized more by HeLa cells and had successfully achieved dual-modal FLI/MRI *in vitro*. Furthermore, *in vivo* T_1-weighted MR imaging indicated that NGd-ACs had superior ability to contrast the liver and tumor with 5-fold lower dosage than previously reported MR contrast agents. Additionally, biodistribution study showed that NGd-ACs were mainly excreted by hepatobiliary metabolism, and the pathological test certificated that they had good biosafety *in vivo*. We propose that the "Albumin Cage" structure would be an efficient strategy to achieve the synergetic enhancement of fluorescence intensity and MR contrast effect by combination of AIE mechanism and prolonging the τ_R of Gd chelates and τ_D of water molecules around Gd chelates.

2. Result and discussion

2.1. Synthesis and Characterization of NGd-ACs

The donor-acceptor (D-A) approach was employed to build the fluorescent moiety, in which dimethoxytriphenylamine and 2H-naphtho[2,3-d] triazole core (NT) were used as the electron-donating and accepting units, respectively. With the introduction of undecylic acid to the triazole part, Gd-DOTA was conjugated into luminogens to obtain the FLI/MRI bimodal probe of NGd. The synthesis and characterizations of NGd in detail were shown in the Supporting Information (Scheme S1 and **Figure 1**a and S1-S7). NGd shows an absorption maximum at 435 nm and fluorescent peak at 570 nm in tetrahydrofuran (THF) (Figure 1b).

Then, we studied its AIE effect by varying the water fraction (f_w) in dimethyl sulfoxide (DMSO)/water mixtures (Figure 1c and 1d). The emission intensity decreases with addition of water into DMSO until f_w reaches 20%, because of the twist intramolecular charge transfer (TICT) process. With the increasing of f_w from 20 to 70%, the fluorescence intensity is gradually enhanced, showing a typical AIE feature, but when f_w is higher than 70%, the fluorescence intensity decreases. This might be ascribed to the formation of aggregates with large sizes, which sink to the bottom and decrease the effective concentration of NGd in the detection beam zone.[13] This was also proved by the decrease in relaxation rate of NGd in the DMSO/water mixtures when f_w is higher than 50% (Figure S8). Notably, introduction of Gd-DOTA into AIE moiety didn't affect its AIE property (Figure S9). Due to the amphiphilic characteristics of NGd, the critical micelle concentration (CMC) of NGd was detected to be 25 μM (Figure S10) by using emission intensity. This reveals that NGd molecules are prone to form aggregates.

To ensure the interaction between NGd molecules and BSA, their binding affinity was firstly estimated by the proton relaxation enhancement.[14] The result demonstrated a high affinity between NGd and BSA with a binding constant of ~1.2×10^5 M^{-1}, and the relaxation rate reaches maximum at the molar ratio of NGd/BSA=2:1 (Figure S11). When NGd were added into BSA aqueous solution, the NGd-BSA complexes would form aggregates. In order to stabilize the disbanded structure of aggregates with suitable size, desolvation and glutaraldehyde coupling were applied to synthesize the NGd-Albumin Cages (NGd-ACs) with the initial feed malar ratio of NGd/BSA=2:1 (Figure 1e). And the encapsulation efficiency of NGd is deduced to be *ca*. 35%. Due to the low CMC, parts of NGd molecules are prone to form aggregates, partially hindering NGd molecules to interact with BSA. The dynamic light scattering (DLS) shows the hydrodynamic diameter of NGd-ACs is about 178 nm, which is similar with the result of ~167 nm measured by transmission electron microscopy (TEM) (Figure 1f). In addition, NGd-ACs are stable in deionized (DI) water, phosphate buffer

solution (PBS), and fetal bovine serum (FBS) (Figure 1g), indicating their high stability in physiological environment, which is feasible for biological applications.

2.2. Synergetic Enhancement of fluorescence and MR signals by NGd-ACs in solution state

To check whether these albumin cages could enhance the fluorescence intensity, the optical properties of NGd-ACs were explored. As shown in **Figure 2**a and S15a, the fluorescence intensity of NGd-ACs is 7- and 5-time higher than that of NGd in DMSO or water, and the fluorescence quantum yield (Φ_F) of NGd-ACs is almost 6 times higher than that of NGd in water or BSA aqueous solution, and more than 3 times higher than that of NGd in DMSO (Figure 2a and Table S1). The obviously enhanced fluorescence intensity and Φ_F of NGd-ACs should be attributed to the RIM of NGd by inserting into BSA cages (Figure 2c). Meanwhile, the fluorescence intensities of NGd in DMSO/water mixture with f_w of 97% and DMSO were almost at the same level, but much lower than that of NGd in DMSO/water mixture with f_w of 70% (Figure S15b). The reason might be that when f_w in the mixture solvent is larger than 70%, the aggregate sediments of NGd become larger and more, further decreasing the effective detection concentration, which leads to the plateau for fluorescence intensity improvement. Because the aggregation of NGd hinders them to interact with BSA effectively, the fluorescence intensity wasn't enhanced even after addition BSA (Figures 2a, 2c, and S12). In addition, the emission peak has an obvious blue-shift for NGd-ACs compared with that of NGd in DMSO (Figure S12a), which is attributed to the noncovalent binding between NGd and BSA through hydrophobic interactions and ion pairing between the cationic groups of gadolinium complex and amino acid residues.[12c] Surprisingly, the fluorescence intensity of NGd-ACs is slightly weaker than that of NGd in DMSO/water mixture with f_w of 70% (Figure S12b). This result indicates that the packing of NGd-ACs was not as tight as that of NGd aggregates in water. The slackened structure of NGd-ACs could generate geometrically

6

confined effect for permitting the water molecules in and out slowly, hence prolonging τ_D of the water molecules, which is beneficial to the improvement of MR contrast effect.

Hereafter, MR contrast effect of NGd-ACs was evaluated and compared with NGd molecules in water or BSA aqueous solution, and clinical contrast agent Gd-DOTA (Figure 2b and S13a). The r_1 of NGd-ACs is 85.1 ± 7.0 mM^{-1}s^{-1} at 0.5 T, which is 17-fold and nearly 8-fold higher than that of Gd-DOTA (4.9 ± 0.5 mM^{-1}s^{-1}) and NGd in aqueous solution (10.9 ± 1.2 mM^{-1}s^{-1}), respectively. This result verifies that the strategy of albumin cage could largely improve the relaxivity of contrast agents. Such a high relaxivity should be ascribed to the elongated τ_{R2} of large size of nanoparticles and τ_{D2} of water molecules trapped in the interval of BSA cages ($\tau_{R1} < \tau_{R2}$ and $\tau_{D1} < \tau_{D2}$, Figure 2c). In addition, the relaxivity of NGd in aqueous solution is higher than that of Gd-DOTA, due to the high molecular weight of NGd and its aggregate state in water.[4a] We further dispersed NGd into the BSA aqueous solution with the molar ratio of 2:1, of which the relaxivity is up to 28.4 ± 1.0 mM^{-1}s^{-1}, 2 times higher than that of NGd in water, but is still 3-fold lower than that of NGd-ACs (Figures 2b and S13a). This consequence could be attributed to the weak interaction of NGd aggregates (slightly elongated τ_{R3}) with BSA and the slightly prolonged τ_{D3} of water molecules because of the "water-blocking" function of albumin ($\tau_{R1} < \tau_{R3} < \tau_{R2}$ and $\tau_{D1} < \tau_{D3} < \tau_{D2}$, Figure 2c). Furthermore, the phantom images of these four groups also prove that NGd-ACs have the brightest contrast effect compared with three other circumstances at the same Gd(III) concentrations (Figure 2d and S13b). From the phantom images, it can be seen that NGd-ACs at a low Gd(III) concentration (0.025 mM) can reach the same brightness of Gd-DOTA at a 16-fold higher concentration (0.4 mM) (Figure S13b), which indicates that a lower dose can generate satisfied effect for NGd-ACs. Therefore, the results of relaxivity and T_1-weighted images illustrate that these albumin cages loading NGd can also largely improve MR contrast effect. Combining with the enhanced fluorescence intensity, NGd-ACs would have great potential as a high-performance FLI/MRI bimodal probe for *in vitro* imaging.

2.3. *In vitro* bimodal FLI/MRI of NGd-ACs

Subsequently, bimodal FLI/MRI of NGd-ACs *in vitro* was explored. T_1-weighted MR images of HeLa cells incubated with NGd-ACs, NGd, and Gd-DOTA with the same Gd(III) concentration of 100 μM were acquired. As shown in **Figure 3**a and 3b, the cells treated with NGd-ACs exhibit strongest positive contrast signal among with those of NGd, Gd-DOTA and PBS groups. Meanwhile, fluorescence intensity of cells incubated with NGd-ACs is brighter than that with NGd. Because Gd-DOTA and PBS are non-emissive, no fluorescence signal is found in the cells treated with them. These results indicate that NGd-ACs can realize *in vitro* bimodal FLI/MRI. To quantify the amount of these probes per cell, inductively coupled plasma mass spectroscopy (ICP-MS) was employed (Figure 3c). The cellular uptake of NGd-ACs, NGd and Gd-DOTA was about 195.6 ± 5.3, 116.1 ± 4.8, 74.5 ± 8.5 fg Gd(III)/cell, respectively. Furthermore, CLSM was employed to observe intracellular accumulation of NGd-ACs and NGd. Obviously, NGd-ACs have been taken up more than NGd by HeLa cells (Figure 3d), illustrating NGd-ACs have a higher cell uptake than other molecules. These results could be attributed to the gp60 albumin receptor distributing on cell surfaces, which can bind albumins to induce clustering of gp60-albumin and association with caveolin-1 and further complete the transcytosis process.[9b] Moreover, 3-(4,5-dimerthylthiazol-2-yl)-2,5-diphenyltetrazolium bromide (MTT) assay showed that HeLa cells had a 100% viability after incubated with NGd-ACs for 24 h even at a Gd(III) concentration of 100 μM, while only 70% viability was obtained when incubated with NGd (Figure S14). This result suggests that NGd-ACs have better biocompatibility than NGd.

2.4. *In vivo* MRI of NGd-ACs

With super performance in T_1-weighted contrast ability in solution state, NGd-ACs were intravenously injected with a low dose of 6 μmol Gd(III)/kg body weight for *in vivo* imaging. T_1-weighted contrast capability of NGd-ACs in liver and tumor of tumor-bearing mice was explored. Clinical contrast agent Gd-DOTA was used as a comparison. T_1-weighted images at

different time points of pre-injection, 1, 3, 7, and 12 h were collected on a 1 T MRI scanner. As shown in **Figure 4**a, compared with per-injection, it can be easily seen a bright signal in liver over time with a peak at 3 h post-injection, and the signal weakened at 12 h post-injection. While for the control group with the same Gd(III) content, slightly bright signal was observed at 1 h post-injection and disappeared quickly due to the rapid renal clearance and weak contrast effect of Gd-DOTA. Subsequently, we analyzed the contrast capability of NGd-ACs in the tumor region. As illustrated in Figure 4b, the positive signals of tumor are getting brighter than that of pre-injection and peak after injection for 7 h. In contrast, there are little positive signals can be seen at different time point after injection of Gd-DOTA apart from inferior bright signal after injection for 1 h. In addition, we also used the values of SNR_{post}/SNR_{pre}[15] and CNR[4c,16] to quantitatively evaluate the change of brightness in liver and tumor. In the liver, the SNR_{post}/SNR_{pre} values of T_1-weighted images are deduced to be 1.6 ± 0.2, 2.7 ± 0.1, 2.1 ± 0.1, 1.4 ± 0.1 at 1, 3, 7, and 12 h after administration of NGd-ACs, respectively (Figure 4c). Moreover, the peak signal after injection for 3 h is ~2.7-fold higher than that of pre-injection. In contrast, the SNR_{post}/SNR_{pre} value of the control group shows a peak of 1.2 ± 0.1 after injection for 1 h, which is more than 2-fold lower than that after injection of NGd-ACs group for 3 h. While the highest CNR for tumor of NGd-ACs after injection for 7 h is ~56%, which is almost 6-fold and more than 3-fold higher than that of pre-scan (~9%) and the control group after injection for 1 h (~17%), respectively (Figure 4d). These results suggest that NGd-ACs hold potential for T_1-weighted tumor imaging because of their large size, which could make them accumulated and retained in the tumor by enhanced permeability and retention (EPR) effect.[17] Importantly, the decreased signals of liver and tumor indicate that NGd-ACs could be gradually cleared from the body after injection for 12 h.

2.5. Biodistribution and biosafety of NGd-ACs

The biodistribution of NGd-ACs in tumor-bearing mice were explored at different time intervals with a dose of 30 μmol Gd(III)/kg body weight. As shown in **Figure 5**a, the liver exhibits the strongest fluorescence signal among these tissues, and intestine, lung, and tumor show faint fluorescence after injection for 3 h. However, after injection for 12 h, the strongest signals were observed in intestine and liver, and no signal was found on the other tissues and tumor. To acquire a quantitative assessment of biodistribution of NGd-ACs, heart, liver, spleen, lung, kidney, intestine and tumors were collected and analyzed for Gd(III) content by ICP-MS. Unlike the *ex vivo* fluorescence signals, NGd-ACs have the highest accumulation in spleen, liver, intestine followed by tumor, lung and kidney (Figure 5b). High accumulation of NGd-ACs in the spleen and liver could be attributed to reticuloendothelial system (RES),[18] whereas enrichment in the intestine likely signifies the clearance of nanoparticles. Surprisingly, with similarly high contents of NGd-ACs in spleen and liver after injection for 3 h (Figure 5b), no fluorescent signal was observed in spleen but strong fluorescent signal could be detected in liver (Figure 5a). This could be ascribed to the different disparities in light absorption and scattering between liver and spleen.[4c,19] Uptake by tumor indicates again that the large size of NGd-ACs extends their residence time in the body, which is conducive to the EPR effect. All organs show significantly decreased Gd(III) content after 12 h, further suggesting the clearance of NGd-ACs. These data confirm that NGd-ACs are mainly taken up by RES and eliminated over time probably by hepatobiliary metabolism.[20]

To evaluate long-term biosafety of NGd-ACs, the serological and histological examinations were carried out. NGd-ACs were injected into healthy BALB/c mice via tail vein at a higher dosage of 30 μmol Gd(III)/kg body weight. For comparison, PBS buffer with the same volume was used under the same experimental conditions. After one month, these mice were all executed and dissected to collect the blood and main organs. The alanine aminotransferase (ALT) and aspartate aminotransferase (AST) are typical serum biochemical indexes. As shown in Figure 5c, these two indexes of mice treated by NGd-ACs are on the similar level to

those of PBS group, suggesting that NGd-ACs have no effect on liver function. Moreover, hematoxylin and eosin (H&E) stained images show that there is no obvious inflammation or cell necrosis in main organs (Figure 5d), indicating that NGd-ACs have good biosafety and will facilitate their practical applications.

3. Conclusion

A facile and straightforward strategy to synergistically enhance Φ_F and r_1 by albumin caged bimodal FLI/MRI probe of NGd-ACs was presented. This probe had good biocompatibility and AIE activity by combination of AIE mechanism (*i.e.* RIM) and prolonging the τ_R of Gd(III) chelates and τ_D of surrounding water molecules. Compared with NGd and clinical contrast agent Gd-DOTA, NGd-ACs exhibited remarkable improvement in both fluorescence and T_1-weighted contrast, which endowed a high-performance bimodal FLI/MRI *in vitro*. As a result, *in vivo* MRI can be acquired using NGd-ACs with a lower dosage than most reported probes. This albumin-cage strategy realizes a "1+1>2" effect for bimodal FLI/MRI, which hopefully inspires researchers to develop biocompatible near-infrared (NIR) or NIR-II FLI/MRI dual-modal probes for the accurate diagnosis and surgical navigation.

Supporting Information

Supporting Information is available from the Wiley Online Library or from the author.

Received: ((will be filled in by the editorial staff))
Revised: ((will be filled in by the editorial staff))
Published online: ((will be filled in by the editorial staff))

References

[1] F. Bray, J. Ferlay, I. Soerjomataram, R. L. Siegel, L. A. Torre, A. Jemal, *CA Cancer J. Clin.* **2018,** 68, 394.

[2] a) M. L. James, S. S. Gambhir, *Physiol. Rev.* **2012,** 92, 897; b) D. S. Karaman, M. P. Sarparanta, J. M. Rosenholm, A. J. Airaksinen, *Adv. Mater.* **2018,** 30, e1703651.

[3] a) V. S. Talanov, C. A. Regino, H. Kobayashi, M. Bernardo, P. L. Choyke, M. W. Brechbiel, *Nano Lett* **2006,** 6, 1459; b) R. Yan, Y. Hu, F. Liu, S. Wei, D. Fang, A. J. Shuhendler, H. Liu, H. Y. Chen, D.Ye, *J. Am. Chem. Soc.* **2019,** 141, 10331.

[4] a) H. Li, G. Parigi, C. Luchinat, T. J. Meade, *J. Am. Chem. Soc.* **2019,** 141, 6224; b) C. Rivas, G. J. Stasiuk, J. Gallo, F. Minuzzi, G. A. Rutter, N. J. Long, *Inorg. Chem.* **2013,** 52, 14284. c) V. S. Harrison, C. E. Carney, K. W. MacRenaris, E. A. Waters, T. J. Meade, *J. Am. Chem. Soc.* **2015,** 137, 9108.

[5] J. Wahsner, E. M. Gale, A. Rodriguez-Rodriguez, P. Caravan, *Chem. Rev.* **2019,** 119, 957.

[6] a) L. Wang, H. Lin, L. Ma, J. Jin, T. Shen, R. Wei, X. Wang, H. Ai, Z. Chen, J. Gao, *Nanoscale* **2017**, 9, 4516; b) K. Ni, Z. Zhao, Z. Zhang, Z. Zhou, L. Yang, L. Wang, H. Ai, J. Gao, *Nanoscale* **2016,** 8, 3768; c) A. Gizzatov, C. Stigliano, J. S. Ananta, R. Sethi, R. Xu, A. Guven, M. Ramirez, H. Shen, A. Sood, M. Ferrari, *Cancer Lett.* **2014,** 352, 97; d) J. S. Ananta, B. Godin, R. Sethi, L. Moriggi, X. Liu, R. E. Serda, R. Krishnamurthy, R. Muthupillai, R. D. Bolskar, L. Helm, M. Ferrari, L. J. Wilson, P. Decuzzi, *Nat.Nanotechnol.* **2010**, 5, 815; e) J. Hu, S. Liu, *Sci. China Chem.* **2018**, 61, 1110.

[7] a) D. Wang, B. Z. Tang, *Acc. Chem. Res.* **2019,** 52, 2559; b) H.-T. Feng, J. W. Y. Lam, B. Z. Tang, *Coord. Chem. Rev.* **2020,** 406, 213142; c) J. Li, J. Wang, H. Li, N. Song, D. Wang, B. Z. Tang, *Chem. Soc. Rev.* **2020,** 49, 1144; d) X. Cai, B. Liu, *Angew.Chem. Int. Ed.* **2020,** 59, 9868; e) H. Zhang, J. Liu, L. Du, C. Ma, N. L. C. Leung, Y. Niu, A. Qin, J. Sun, Q. Peng, H. H. Y. Sung, I. D. Williams, R. T. K. Kwok, J. W. Y. Lam, K. S. Wong, D. L. Phillipsd, B. Z. Tang, *Mater. Chem. Front.* **2019**, 3, 1143.

[8] Y. Chen, M. Li, Y. Hong, J. W. Y. Lam, Q. Zheng, B. Z. Tang, *ACS Appl. Mater. Intefaces* **2014,** 6, 10783.

[9] a) F. Kratz, *J. Control. Release* **2008**, *132*, 171; b) D. Sleep, J. Cameron, L. R. Evans, *Biochim. Biophys. Acta.* **2013**, *1830*, 5526.

[10] a) X. Liu, C. Wang, Z. Liu, *Adv. Healthc. Mater.* **2018**, *7*, e1800913; b) Z. Liu, X. Chen, *Chem. Soc. Rev.* **2016**, 45, 1432.

[11] a) P. Caravan, *Acc. Chem. Res.* **2009**, *42*, 851; b) E. Boros, P. Caravan, *J. Med. Chem.* **2013**, *56*, 1782.

[12] a) W. Qin, D. Ding, J. Liu, W. Z. Yuan, Y. Hu, B. Liu, B. Z. Tang, *Adv. Funct. Mater.* **2012**, *22*, 771; b) S. Gao, G. Wei, S. Zhang, B. Zheng, J. Xu, G. Chen, M. Li, S. Song, W. Fu, Z. Xiao, W. Lu, *Nat. Commun.* **2019**, 10, 2206; c) S. Wang, F. Hu, Y. Pan, L. G. Ng, B. Liu, *Adv. Funct. Mater.* **2019**, *29*, 1902717.

[13] T. He, N. Niu, Z. Chen, S. Li, S. Liu, J. Li, *Adv. Funct. Mater.* **2018**, *28*, 1706196.

[14] A. C. Esqueda, J. A. Lopez, G. Andreu-de-Riquer, J. C. Alvarado-Monzon, J. Ratnakar, A. J. Lubag, A. D. Sherry, L. M. De Leon-Rodriguez, *J. Am. Chem. Soc.* **2009**, *131*, 11387.

[15] a) L. Wang, H. Lin, X. Chi, C. Sun, J. Huang, X. Tang, H. Chen, X. Luo, Z. Yin, J. Gao, *Small* **2018**, *14*, e1801612; b) Z. Zhou, L. Wang, X. Chi, J. Bao, L. Yang, W. Zhao, Z. Chen, X. Wang, X. Chen, J. Gao, *ACS Nano* **2013**, *7*, 3287.

[16] Z. Zhou, D. Huang, J. Bao, Q. Chen, G. Liu, Z. Chen, X. Chen, J. Gao, *Adv. Mater.* **2012**, *24*, 6223.

[17] a) H. Kang, S. Rho, W. R. Stiles, S. Hu, Y. Baek, D. W. Hwang, S. Kashiwagi, M. S. Kim, H. S. Choi, *Adv. Healthc. Mater.* **2020**, *9*, e1901223; b) K. Greish, *Methods Mol. Biol.* **2010**, *624*, 25.

[18] K. Yang, J. Wan, S. Zhang, Y. Zhang, S. T. Lee, Z. Liu, *ACS Nano* **2011**, *5*, 516.

[19] N. Sharma, M. A. Saifi, S. B. Singh, C. Godugu, *Nanotoxicity* **2020**, 41.

[20] M. Longmire, P. L. Choyke, H. Kobayashi, *Nanomedicine* **2008**, *3*, 703.
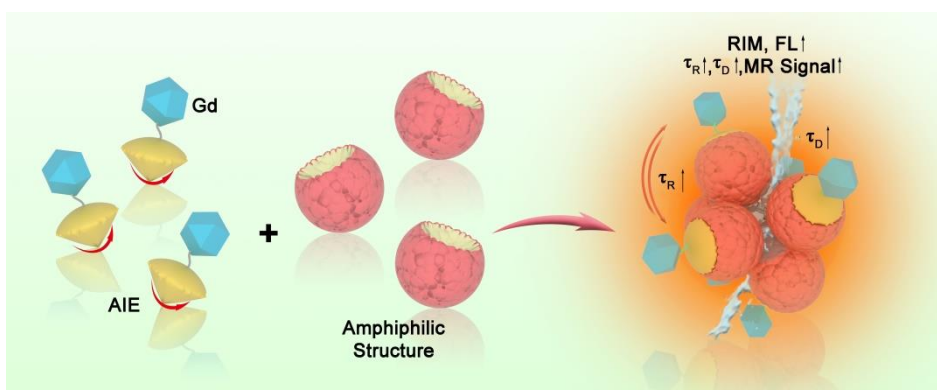
Scheme 1. Schematic illustration of the amphiphilic structures loaded with AIE-Gd molecules that generate supramolecular nanoconstructs with enhanced fluorescence emission and improved MR signal.
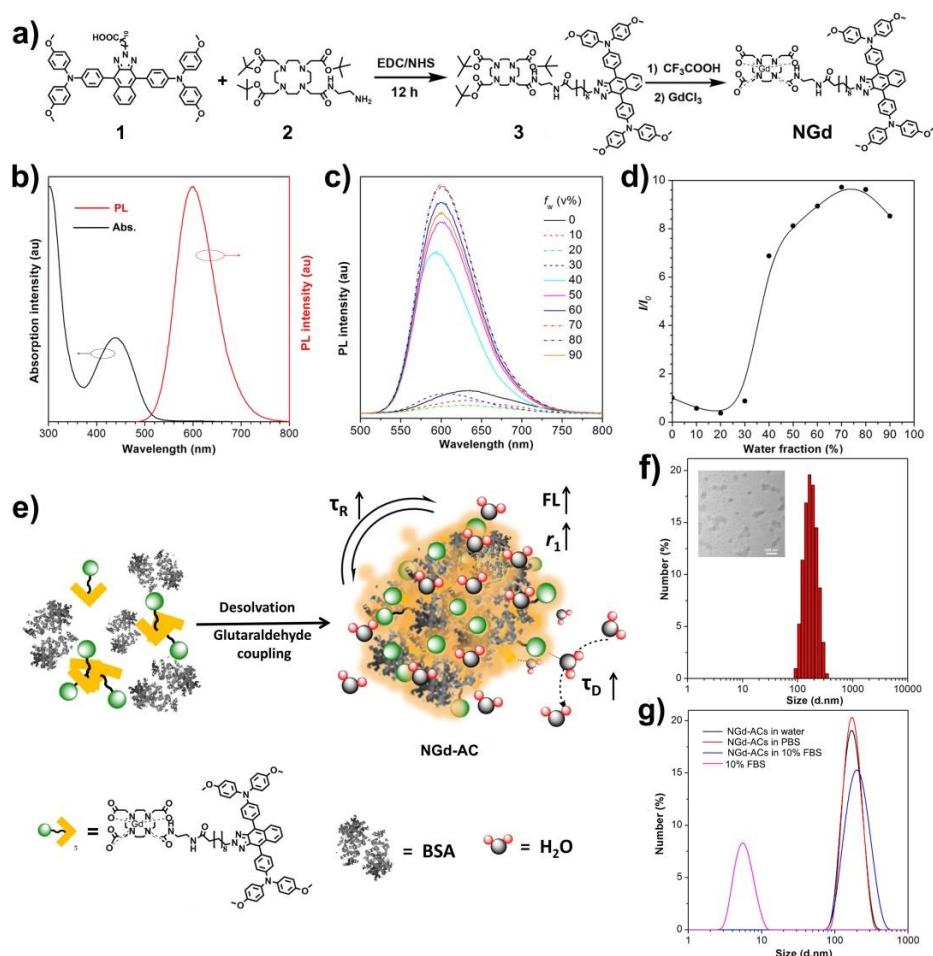
Figure 1. (a) Synthetic route to NGd: 1) deprotection of the *tert*-butyl groups with trifluoroacetic acid (CF$_3$COOH), and then 2) coordination with GdCl$_3$. (b) Absorption and photoluminescence (PL) spectra of NGd in THF. (c) PL spectra of NGd (10 μM) in DMSO/water mixtures with different water fraction (f_w). (d) Plots of the relative emission intensity of NGd *versus* water fraction. I_0 and I are the peak values of PL intensities of NGd (10 μM) in DMSO/water mixtures with different f_w. (e) Schematic illustration of the synthesis of NGd-Albumin Cage (NGd-AC) and the mechanism of synergistic FLI/MRI enhancement. (f) Hydrodynamic diameter of NGd-ACs in water measured by DLS. Inset: TEM images of NGd-ACs. (g) DLS results of NGd-ACs in DI water, PBS, and 10% FBS, respectively, and 10% FBS alone.

15
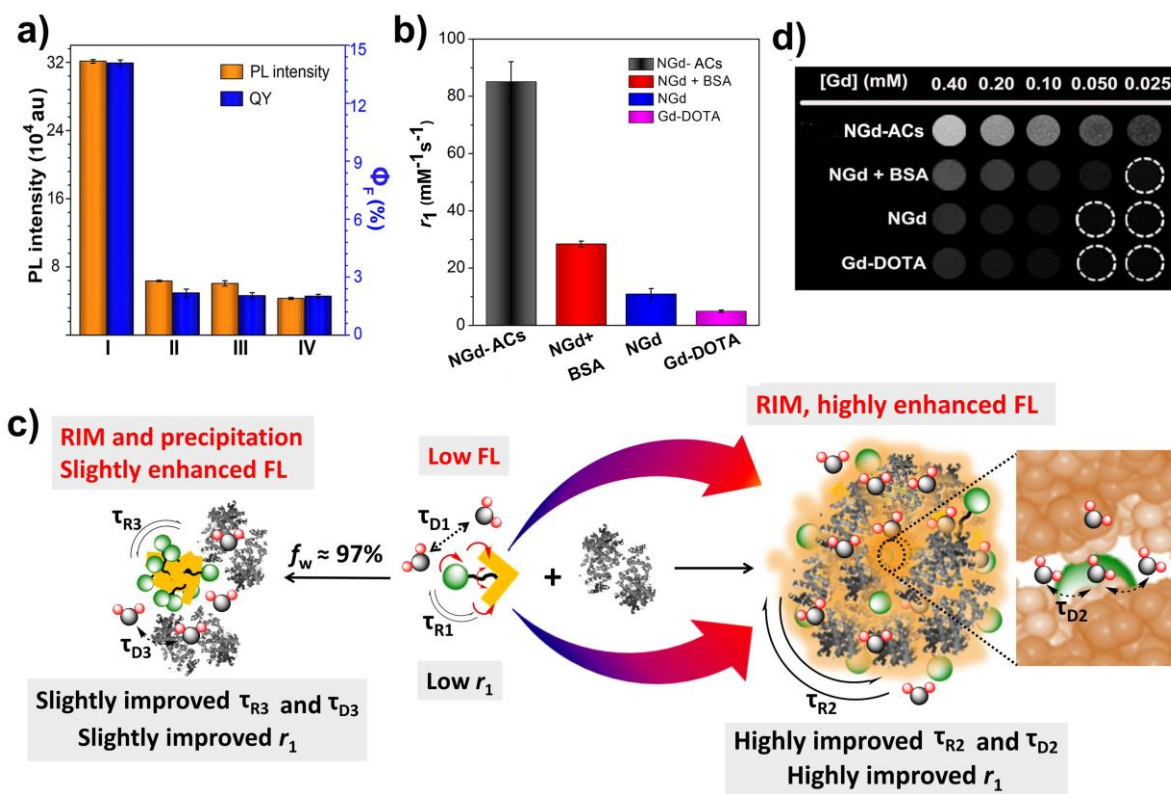
Figure 2. Exploration of fluorescence and relaxation effect. (a) PL intensity and fluorescence quantum yield (Φ_F) of (I) NGd-ACs and (II) NGd molecules in BSA solution (the molar ratio of NGd/BSA = 2:1), (III) water, and (IV) DMSO, respectively. (b) T_1 relaxivities of NGd-ACs, NGd in BSA aqueous solution (the molar ratio of NGd/BSA = 2:1), NGd in water, and Gd-DOTA at 0.5 T, respectively. (c) Illustration of mechanism of simultaneous enhancement of fluorescence and relaxivity. τ_{R1}, τ_{R2}, and τ_{R3} refer to rotational correlation time of NGd molecules, NGd-ACs, and NGd aggregates in BSA aqueous solution, respectively; τ_{D1}, τ_{D2}, and τ_{D3} refer to diffusion correlation time of water molecules around them, respectively. (d) Phantom images of NGd-ACs, NGd in BSA aqueous solution, NGd in water, and Gd-DOTA at different Gd(III) concentrations, respectively.
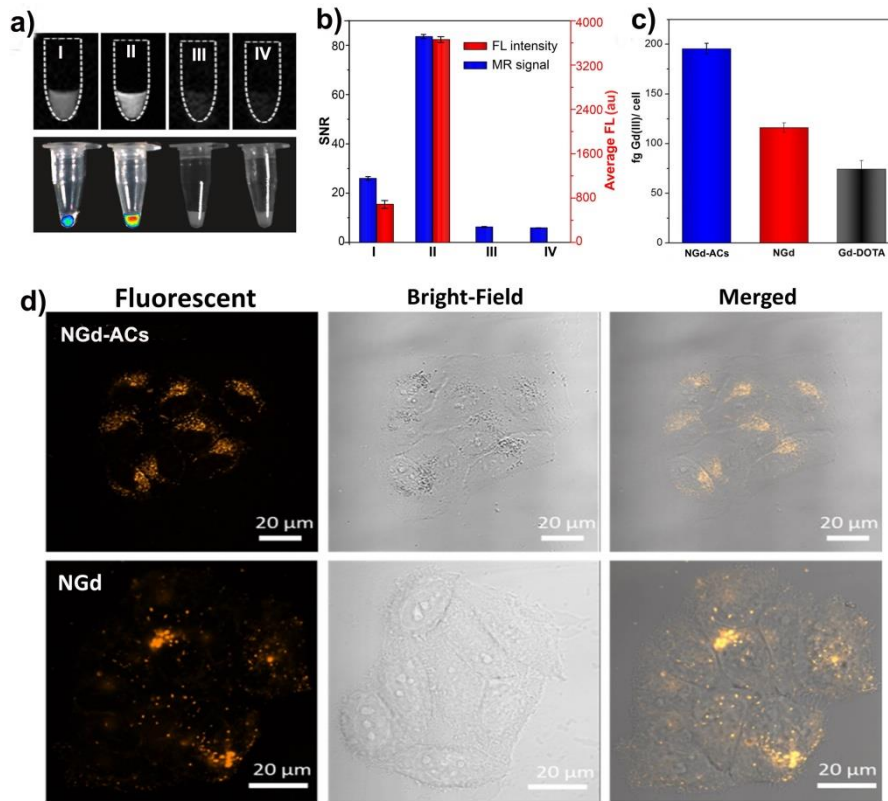
Figure 3. FLI and MRI *in vitro*. (a) T_1-weighted MRI (up) and fluorescence (down) images of cell pellets. (b) Comparison of signal to noise ratio (SNR) of T_1-weighted images (0.5 T, blue) and the average FL intensity (red) of cell pellets in (a). I, II, III and IV refer to HeLa cells incubated with NGd, NGd-ACs, Gd-DOTA, and PBS, respectively. (c) Quantification of cellular uptake of NGd-ACs, NGd, and Gd-DOTA, respectively. (d) CLSM images of HeLa cells incubated with NGd-ACs and NGd. Scale bar: 20 μm, [NGd-ACs] = [NGd] = 10 μM.

17
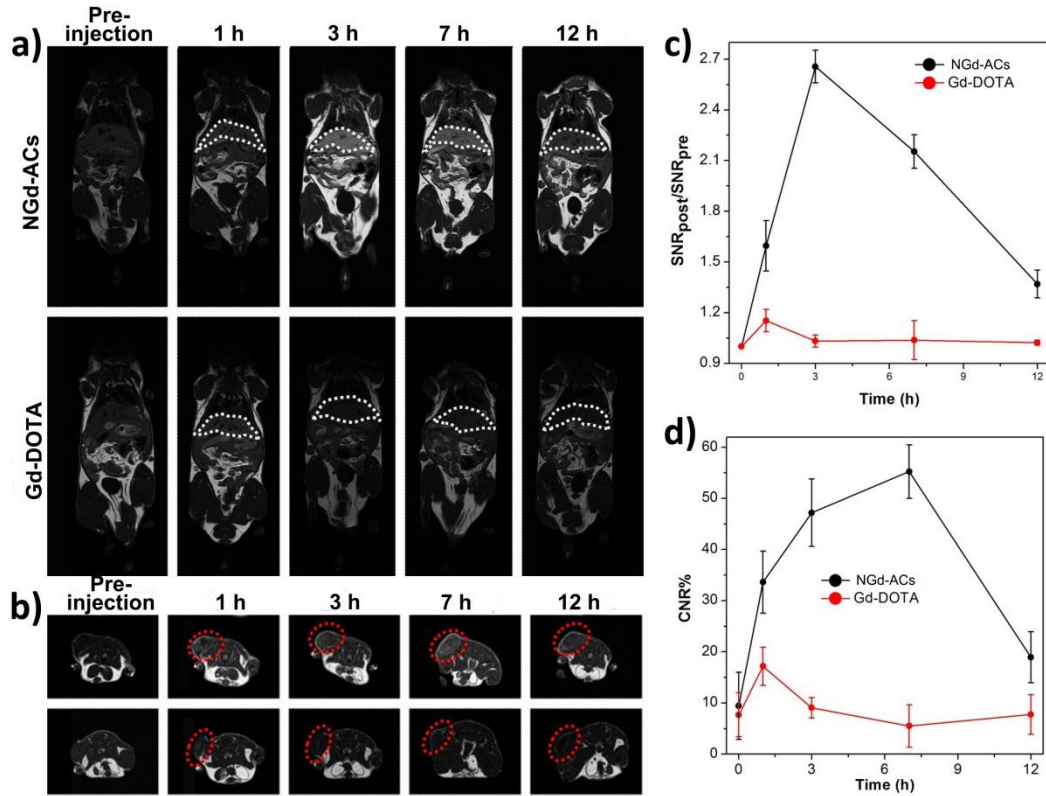
Figure 4. *In vivo* T_1-weighted MRI and analysis of mice after intravenous injection of NGd-ACs or Gd-DOTA. (a) MRI of liver with the dosage of 6 μM Gd(III)/Kg body weight before and after intravenous injection at 1, 3, 7, and 12 h, respectively. The white dotted lines refer to liver. (b) MRI of tumor before and after intravenous injection of NGd-ACs (up) and Gd-DOTA (down) at 1, 3, 7, and 12 h, respectively. The red dotted circles refer to tumor. (c) Quantitative analysis of signal changes (SNR ratio) in liver versus treating time. (d) Contrast-to-noise ratios (CNR) of tumor and tissue contrast before and after injection of the probes at 1, 3, 7, and 12 h, respectively. CNR = |SNR$_{tumor}$ - SNR$_{muscle}$/SNR$_{muscle}$.

18
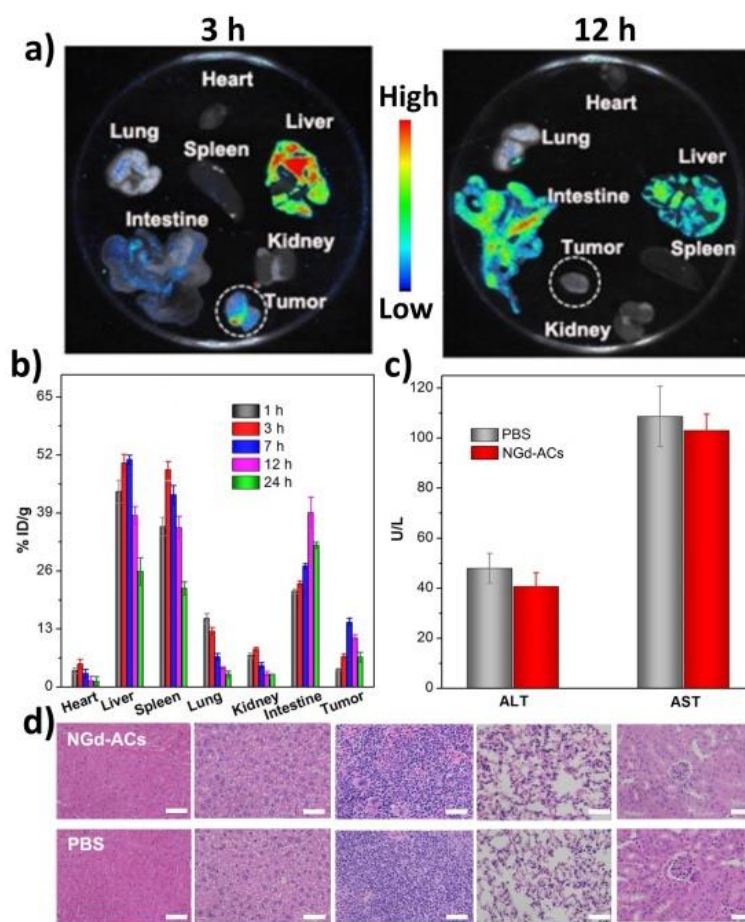
Figure 5. Biodistribution and biosafety assessment. (a) *Ex vivo* fluorescence images of main tissues (heart, liver, spleen, lung, kidney and intestine) and tumor from mice at 3 and 12 h post-injection of NGd-ACs. (b) Biodistribution of NGd-ACs at 1, 3, 7, and 12 h after injection in tumor-bearing mice evaluated by ICP-MS. (c) Serological test results of mice injected with NGd-ACs (30 μmol Gd(III)/kg body weight, PBS was as the control). (d) H&E stained tissue sections from mice after intravenous injection of NGd-ACs (30 μmol Gd(III)/kg body weight) for 30 days, and PBS was used as a control. Scale bar: 50 μm for all images.

The table of contents entry:

A facile and straightforward strategy to synergistically enhance fluorescence quantum yield and T_1 relaxivity by albumin caged bimodal FLI/MRI probe of NGd-ACs is presented. This albumin cage organically integrates the mechanism of AIE and the prolonged rotation correlation time of gadolinium complex and diffusion correlation time of the surrounding water molecules, achieving an effect of 1+1 **>** 2.

Keyword: albumin cage, fluorescence, magnetic resonance signal, aggregation-induced emission, synergetic enhancement

Lirong Wang,[1] Qing Wan,[1] Rongyuan Zhang,[6] Bo Situ,[3] Kaiyuan Ni,[5] Jinhao Gao,[2] Zhiming Wang,[1,*] Anjun Qin,[1,*] Ben Zhong Tang[1,4]

Synergetic Enhancement of Fluorescence and Magnetic Resonance Signals Assisted by Albumin Cage
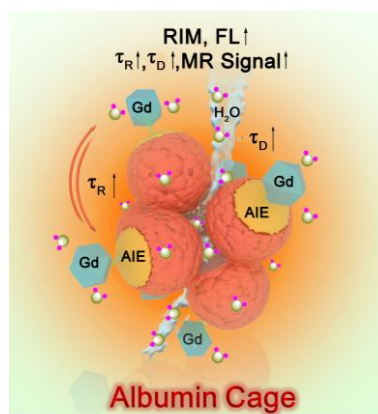
Supporting Information

Synergetic Enhancement of Fluorescence and Magnetic Resonance Signals Assisted by Albumin Cage

Lirong Wang,[1] Qing Wan,[1] Rongyuan Zhang,[6] Bo Situ,[3] Kaiyuan Ni,[5] Jinhao Gao,[2] Zhiming Wang,[1,]* Anjun Qin,[1,]* Ben Zhong Tang[1,4]

Materials and Methods

All chemicals, unless otherwise noted, were purchased from commercial sources and used without further purification. $GdCl_3$, 1-ethyl-3-(3-dimethylamino-propyl) carbodiimide hydrochloide (EDC) and *N*-hydroxysulfo-succinimide (NHS) were purchased from Alfa Aesar. 1,4,7,10-Tetra-azacyclododecane (min. 98% CYCLEN) was purchased from Strem Chemicals Inc.. Ultra-filtration units (Amicon Ultra 15 mL Filters with 30 kDa nominal molecular weight cutoff) were purchased from Merck Millipore Corp. [4-(bis(4-methoxyphenyl)amino)phenyl]boronic acid was obtained from Soochiral Chemical Science & Technology Co., Ltd. 2,3-Dihydronaphthalene-2,3-diamine was purchased from Bide Pharmatech Ltd. Zinc chloride were obtained from Alfa Aesar. Sodium nitrite, potassium carbonate and sodium hydroxide were purchased from Aladdin Co., Ltd. Tetrakis(triphenylphosphine)palladium and 11-bromoundecanoic acid were obtained from Energy Co., Ltd.

^{1}H and ^{13}C NMR spectra were measured on a Bruker AV 500 spectrometer. High-resolution mass spectra (HR-MS) were recorded on a Acquity UPLC/XEVO G2-XS QTOF operating in MALDI-TOF mode. UV-vis absorption spectra were measured on a Shimadzu UV-2600 spectrophotometer. Photoluminescence spectra were recorded on a Horiba Fluoromax-4 spectrofluorometer. Photoluminescence (PL) quantum yields were measured using a Hamamatsu absolute PL quantum yield spectrometer C11347 Quantaurus_QY. Confocal laser scanning microscope (CLSM) characterization was conducted with a Zeiss LSM 710

(Germany) confocal laser scanning biological microscope. The absorbance for MTT analysis was recorded on a Thermo Fisher microplate reader (USA) at a wavelength of 490 nm. The element analysis of Gd was also carried out by inductively coupled plasma atomic emission spectroscopy (ICP-AES) or inductively coupled plasma mass spectroscopy (ICP-MS). The morphology and structure of NGd-BSA NPs with phosphotungstic acid staining (1 wt. %) were characterized by transmission electron microscopy (TEM) using a JEOL JEM-2100 transmission electron microscope. The dynamic light scattering (DLS) measurements were performed on a Malvern Zetasizer nano ZS instrument. The T_1 relaxation time measurements were performed on 0.5 T NMI20-Analyst NMR Analyzing & imaging system (Niumag Corporation, Shanghai, China), *In vivo* MR imaging was performed on a 1 T MRI System (Aspect M3^{TM}, Israel). *Ex vivo* fluorescence imaging was carried out on Bruker FX Pro.
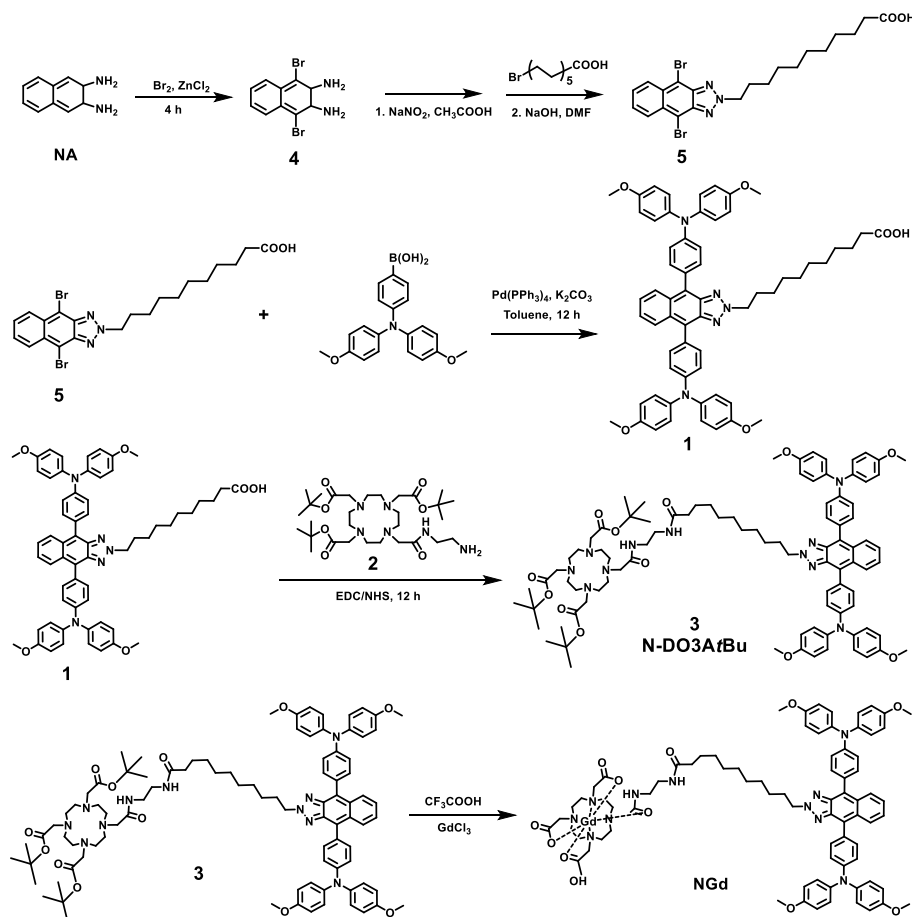
Scheme S1 Synthetic routes to NGd

Synthesis of Intermediate 4

The intermediate **4** was prepared by the bromination reaction according to previous literature.[1] A mixture of 1.7 mL of bromine (10.4 g, 43 mmol) and 50 mL of glacial acetic acid was gradually added into 70 mL of glacial acetic acid solution containing 2,3-dihydronaphthalene-2,3-diamine (NA) (2.5 g, 16 mmol), and then the solution was stirred at room temperature for 4 h. The deionized water was added into solution, and the precipitate was filtered off and washed with glacial acetic acid and water. The brown powder was obtained after drying (3.8 g, 81%).

Synthesis of Intermediate 5

The intermediate **5** was synthesized according to previous literature.[2] 15 mL of NaNO$_2$ aqueous solution (3.0 g, 33.0 mmol) was added dropwise to 30 mL of glacial acetic acid containing compound **4** (3.16 g, 10 mmol). After vigorous stirring for 30 min at room

temperature, the precipitate was filtered off and washed with water to obtain brown powder. The crude product was directly used without further purification. The obtained brown powder (2.5 g, 7.6 mmol) was dissolved in dry DMF (30 mL) and NaOH (11.4 mmol, 456 mg) was added with vigorous stirring within 1 h. 11-Bromoundecanoic acid (4.1 g, 15.2 mmol) in DMF (20 mL) was added dropwise and the solution was stirred at room temperature for 24 h. Afterward, the solution was adjusted to faintly acid by dilute hydrochloric acid. Then, the solution was extracted with DCM/water to remove DMF, the organic layer was dried over anhydride $MgSO_4$. After filtration and solvent evaporation, the crude product was purified by column chromatography using ethyl acetate/petroleum ether mixture as eluent to afford orange powder (2.8 g, 73%). ^1H NMR (DMSO-d_6, 500 MHz): δ 11.88 (s, 1H), 8.33 (m, 2H), 7.70 (m, 2H), 4.91 (t, 2H), 2.17 (m, 4H), 1.32-1.20 (m, 14 H). ^{13}C NMR (DMSO-d_6, 500 MHz): δ 174.9 142.4, 130.9, 128.1, 126.9, 108.5, 58.1, 34.1, 29.8, 29.2, 29.1, 28.9, 28.7, 26.3, 24.9. HR-MS calculated for $C_{21}H_{26}Br_2N_3O_2$ [M+H]$^+$ m/z: 510.0392, found: 510.0387.

Synthesis of Compound 1

The Compound **1** was synthesized by Suzuki coupling reaction. The mixture of [4-(bis(4-methoxyphenyl)amino)phenyl]boronic acid (2.1 g, 6 mmol), intermediate **5** (1.53 g, 3 mmol) and $Pd(PPh_3)_4$ (116 mg, 0.1 mmol) were dissolved in 20 mL toluene and 12 mL K_2CO_3 (2 M) aqueous solution. Then, the mixture was refluxed under nitrogen for 24 h. After solvent evaporation, the crude product was purified by column chromatography using ethyl acetate/petroleum ether mixture as eluent to afford orange powder (1.7 g, 89%). ^1H NMR (DMSO-d_6, 500 MHz): δ 8.04 (d, 2H), 7.45 (d, 2H), 7.35 (d, 2H), 7.19 (d, 2H), 6.96 (d, 2H), 8.92 (d, 2H), 4.80 (t, 2H), 3.76 (s, 12 H), 1.98 (t, 2H), 1.87 (t, 2H), 1.26-1.15 (m, 14H). ^{13}C NMR (DMSO-d_6, 500 MHz): δ 174.9, 156.5, 148.3, 141.8, 140.3, 133.6, 132.8, 132.5, 132.3, 132.0, 131.9, 129.2, 127.8, 118.3, 115.5, 55.6, 34.1, 30.1, 29.2, 28.9, 26.4, 24.9. HR-MS calculated for $C_{61}H_{62}N_5O_6$ [M+H]$^+$ m/z: 960.4700, found: 960.4717.

Synthesis of Compound 3 (N-DO3AtBu)

Compound **1** (100 mg, 0.1 mmol), 1-(3-dimethylaminopropyl)-3-ethylcarbodiimide hydrochloride (EDC) (28.7 mg, 0.15 mmol), *N*-hydroxysuccinimide (NHS) (17.3 mg, 0.15 mmol) were dissolved in dry DMF (10 mL) and stirring at room temperature for 1 h. The DMF solution (2 mL) of compound **2** [tri-tert-butyl 2,2',2''-(10-(2-((2-aminoethyl) amino)-2-oxoethyl)-1,4,7,10-tertraazacyclododecane-1,4,7-triyl)triacetate, 67.5 mg, 0.11 mmol], which was synthesized according to the previous procedures,[3] was added and the mixture was stirred at 50 °C for 10 h. Afterward, the solution was extracted with DCM/water, the organic layer was dried over anhydride $MgSO_4$. After filtration and solvent evaporation, the crude product was purified by column chromatography using methanol/DCM mixture as eluent to afford light-yellow powder compound **3** (99.5 mg, 64%). ^1H NMR (500 MHz, CD_2Cl_2): δ 8.14 (dd, 2H), 7.49 (d, 4H), 7.30 (dd, 2H), 7.21 (d, 8H), 7.07 (d, 4H), 6.91 (d, 8H), 4.80 (t, 2H), 3.81 (s, 12H), 3.34 – 3.19 (m, 4H), 2.83 – 2.08 (m, 26H), 1.84 (s, 2H), 1.71 – 0.96 (m, 41H). ^{13}C NMR (500 MHz, CD_2Cl_2): δ 177.82, 177.57, 175.02, 172.94, 170.64, 157.45, 149.82, 143.82, 141.63, 133.36, 131.33, 129.18, 128.42, 128.04, 127.87, 127.72, 125.63, 121.71, 120.37, 116.12, 91.90, 56.78, 54.75, 45.25, 43.64, 39.49, 37.49, 36.54, 35.73, 33.21, 32.45, 31.67, 31.01, 30.96, 30.86, 30.70, 30.59, 30.44, 30.36, 29.98, 29.24, 27.95, 26.24, 24.01, 15.93, 15.20. HR-MS calculated for $C_{91}H_{118}N_{11}O_{12}$ $[M+H]^+$ *m/z*: 1556.8961, found: 1556.8981.

Synthesis of NGd

Compound 3 (90 mg, 0.06 mmol) was dissolved in 3 mL trifluoroacetate acid (TFA) at room temperature for deprotection. After stirring for 6 h, excess TFA was removed by rotary evaporation. And then, the resultant brown oily product was dissolved in methanol, and the pH of the solution was adjusted to 5~6 with dilute sodium hydroxide solution. Anhydrous gadolinium chloride (24 mg, 0.09 mmol) was dissolved into 3 mL methanol, and added dropwise into the above brown solution. After reaction overnight at 60 °C, the methanol was removed by evaporation. The crude product was re-dissolved in DCM, and the excess

gadolinium ions were washed off with water to obtain the brown solid product (92.5 mg, 90%). HR-MS (m/z) calculated for $C_{79}H_{91}GdN_{11}O_{12}$ $[M+H]^+$ m/z: 1542.6011, found: 1542.6017.

Binding constant of NGd to BSA

The binding constant of NGd to BSA was assessed by proton relaxation enhancement (PRE), which is commonly used to determine affinity constant of Gd(III) complexes to serum albumin.[4] The water proton relaxation time was measured with the increasing concentrations of BSA in PBS buffer while the concentration of NGd keeps unchanged at 10 μM. The binding constant was calculated according to the following equations 1 to 3.
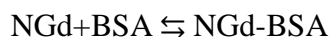
$$NGd + BSA \leftrightarrows NGd\text{-}BSA$$

$$K_D = \frac{[NGd][BSA]}{[NGd-BSA]} \qquad (1)$$

$$\varepsilon^* = \frac{(1/T_1)_{NGd-BSA} - (1/T_1)_{BSA}}{(1/T_1)_{NGd-PBS} - (1/T_1)_{PBS}} \qquad (2)$$

$$\varepsilon^* = \frac{\varepsilon_{max}[BSA]_t + K_D}{K_D + [BSA]_t} \qquad (3)$$

Where, K_D is the binding dissociation constant; [NGd-BSA] is the concentration of NGd-BSA complex; [NGd] is the concentration of free NGd in solution; [BSA] is the concentration of free BSA in solution; $[BSA]_t$ is the total concentration of BSA; ε^* is the enhancement factor; ε_{max} is the maximum value that the enhancement factor can reach extrapolated to the scenario where all the contrast agent molecular are almost bound to BSA; $(1/T_1)_{NGd-BSA}$, $(1/T_1)_{BSA}$, $(1/T_1)_{NGd-PBS}$, $(1/T_1)_{PBS}$ are the relaxation rates of water protons in NGd plus BSA, BSA alone, NGd plus PBS, and PBS alone, respectively.

Synthesis of NGd-ACs

NGd molecules were dissolved in DMSO at a Gd(III) concentration of 16.7 mM and kept in 4 °C refrigerator. NGd-ACs were synthesized by desolvation followed by glutaraldehyde coupling.[3a,5] 181.4 μL of NGd was diluted to 20 mL THF and dropwise added into 50 mL of

BSA (~20 mg/mL) aqueous solution. The molar ratio of BSA/NGd is 1:2. The resultant mixture was stirred for 30 min at room temperature. Under a stirring at 400 rpm, additional THF was dropwise added to the above mixture until the solution became slightly turbid. Then 100 μL of 2.5% glutaraldehyde aqueous solution was added, and the reaction was covered with aluminum foils and stirring at room temperature. After reaction for 4 h, the mixture was concentrated in vacuum to remove organic solutions at room temperature. And the NGd-ACs were purified three times by ultrafiltration with Amicon centrifuge tubes (MWCO =30 kDa) and re-dispersion in DI-water under sonication. The Gd(III) concentration was measured by inductively coupled plasma atomic emission spectroscopy (ICP-AES). The encapsulation efficiency (EE) of NGd was calculated according to the following equation 4.

$$EE = \frac{\text{Mass of encapsulated NGd}}{\text{Total mass of added NGd}} \times 100\%$$
(4)

T_1 Relaxivity and MR Phantom Study

The T_1 relaxation times of NGd-ACs, NGd in BSA aqueous solution (molar ratio of BSA/NGd = 1:2), NGd in water, and Gd-DOTA were measured at 0.5 T MRI scanner with the Gd(III) concentration of 0.40, 0.20, 0.10, 0.05, and 0.025 mM, respectively. Then, the values of r_1 were calculated through the curve fitting of relaxation rates (s^{-1}) versus the Gd(III) concentration (mM). Meanwhile, T_1-weighted phantom images were carried out with TR/TE = 100/0.004 ms.

Cell culture

HeLa cells were cultured in Dulbecco's modified eagle medium (DMEM) containing 10% fetal bovine serum at 37 ^{o}C in a humidified environment containing 5% CO_2.

Confocal Microscopy

HeLa cells were seeded at a density of 5×10^4 cells per plate on a 35 mm dish. Cells were incubated with the same Gd(III) concentration (10 μM) of NGd-ACs and NGd for 24 h. Cells were washed twice with PBS and fresh media was added. Cells were imaged using a Zeiss LSM 710 confocal laser scanning with the excitation of 405 nm and emission of 500-600 nm.

Cell viability

The cytotoxicity of NGd-ACs and NGd were assessed by the 3-(4, 5-dimethylthiazol-2-y1)-2, 5-diphenyltetrazolium bromide (MTT) method. HeLa cells were firstly seeded into a 96-well plate at a density of 1×10^4 cells per well in DMEM, and incubated for 24 h. Then the media were replaced by the different Gd(III) concentrations of NGd-ACs and NGd (0.78, 1.56, 3.13, 6.25, 12.5, 25, 50, 100 μM) and cells were incubated for another 24 h. After incubation, the culture media were removed and each well was filled with 100 μL of new culture media containing MTT (0.5 mg/mL) and incubation for additional 4 h. Then the media was discarded and each well was added with another 100 μL DMSO. The OD490 value (Abs.) of each well was measured by microplate reader immediately. Cell viability was expressed by the ratio of OD490 values of the cells incubated with NGd-ACs or NGd suspension to that of the cells incubated with culture medium only.

Cell MR/FL imaging and cell uptake

HeLa cells at a density of 5×10^6 per dish were seeded into four tissue culture dishes respectively. After incubation for 24 h, these media were replaced by the same Gd(III) concentration (100 μM) of media containing NGd-ACs, NGd, and Gd-DOTA respectively, PBS was used as blank group. The cells of four groups were washed with PBS three times and harvested into 200 μL microcentrifuge tube, respectively. T_1-weighted phantom images of cells were obtained on a 0.5 T NMR120-Analyst NMR system with parameters: TR = 100 ms and TE = 5.3 ms. The regions of interest were measured by ImageJ. After that, fluorescence images of these samples were collected using BIO-RAD ChemiDoc™ MP gel imaging system with white light excitation.

After imaging testing, the collected cells were nitrified by 70% (wt/vol) HNO$_3$ at 100 °C overnight. The digested solutions were collected and diluted to 10 mL. The Gd content in each sample was analyzed by ICP-MS.

In vivo MR Imaging

All animal studies were approved by Institutional Animal Care and Use Committee (IACUC) of South China University of Technology.

MR imaging of BALB/c tumor bearing mice (6 weeks) were carried out on a 1 T MR scanner (Aspect M3^{TM}, Israel). NGd-ACs were intravenously injected into mice with a dose of 6 μmol Gd/kg body weight. Gd-DOTA as clinically used MRI contrast agent was employed as control. T_1-weighted images were acquired at different time points after injection. All the images were obtained using spin-echo sequence (SE) with parameters as follows: TR/TE = 330/12.5 ms, slice thickness = 1 mm, FOV = 30 × 90.

Ex vivo FL imaging

BALB/c tumor bearing mice were intravenously injected with 6 μmol Gd(III)/kg body weight. Organs (heart, liver, spleen, lung, kidney, intestine) and tumors were harvested after injection for 3 and 12 h. Organs were imaged on the Bruker FX Pro with λ_{ex} = 410 nm and λ_{em} = 535 nm.

Biodistribution in Tumor-Bearing Mice

BALB/c tumor bearing mice were injected with NGd-ACs and NGd at the same dose of 30 μmol Gd(III)/kg body weight and were sacrificed after injection for 1, 3, 7, and 24 h (n = 4/group). Tumors and major organs (heart, liver, spleen, lung, kidney, intestine) were collected and weighed, and chemically digested using the method of microwave shock with HNO_3/H_2O_2 (3:1 v/v) at 100 ºC. Each digested sample was diluted to a certain volume with 2% HNO_3 and filtered through a 0.22 μm pore filter membrane. The Gd(III) concentrations in these samples were measured using ICP-MS. The final Gd(III) concentrations were expressed as the percentage of the injected dose per gram tissue (% ID/g).

Serological test and Histological Examination

BALB/c mice were intravenous injected with NGd-ACs at the dosage of 30 μmol Gd(III)/kg mouse body weight as the experimental group (n = 4). The mice of the control group (n = 4) were injected with the same volume of PBS solution. After 30 days, blood was

collected by heart to evaluate the liver function, including alanine aminotransferase (ALT) and aspartate aminotransferase (AST). In addition, the main organs including heart, liver, spleen, lung, and kidneys were collected, sectioned and stained with hematoxylin and eosin. The histological sections were analyzed for the study of *in vivo* toxicity.
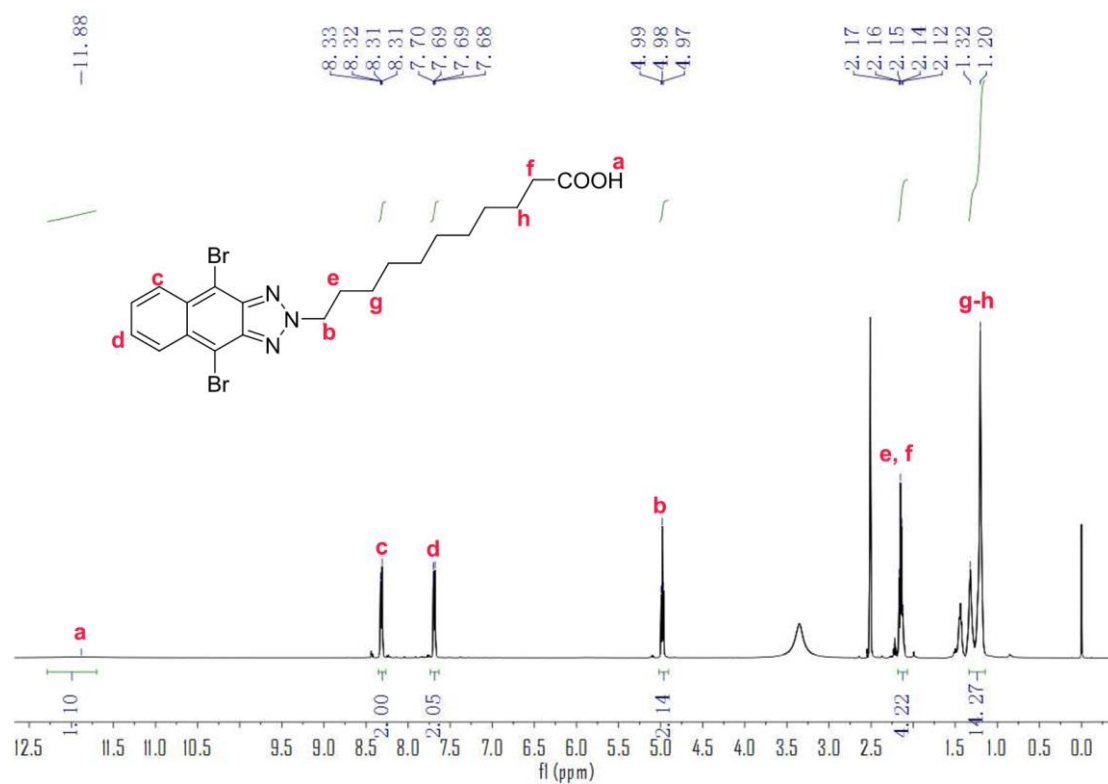
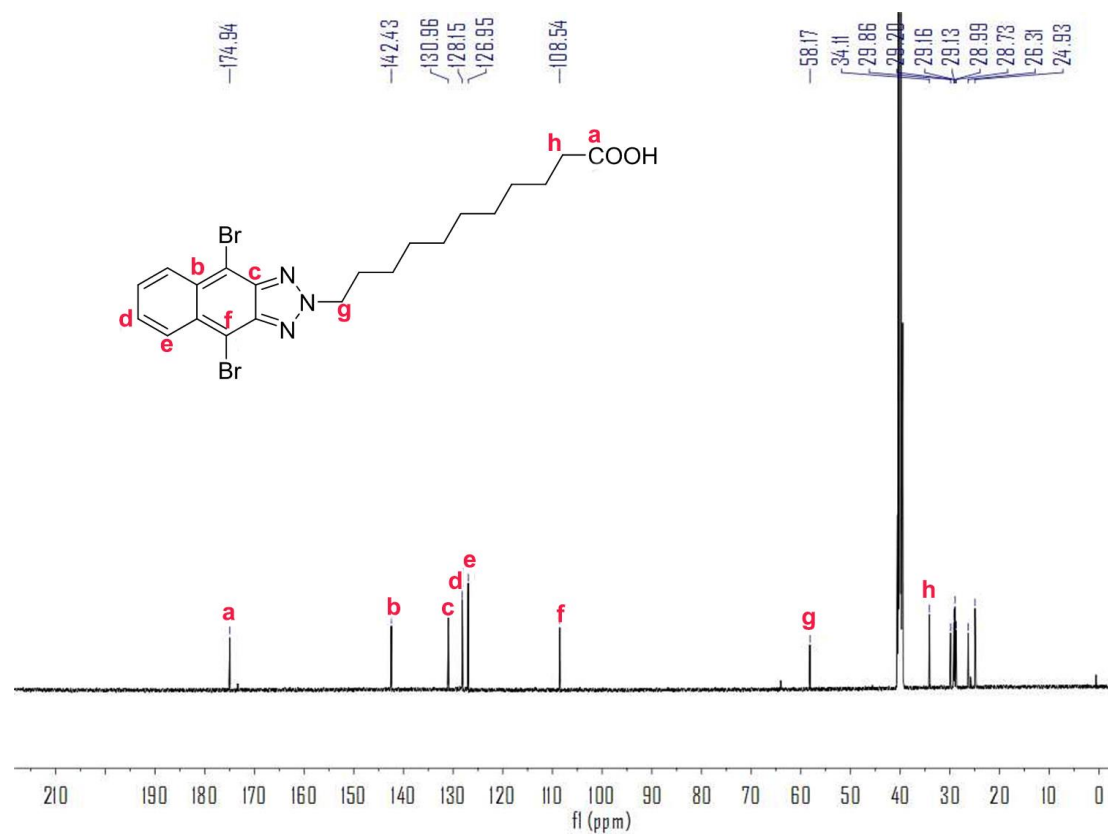**Figure S1.** ¹H NMR of Intermediate **5**
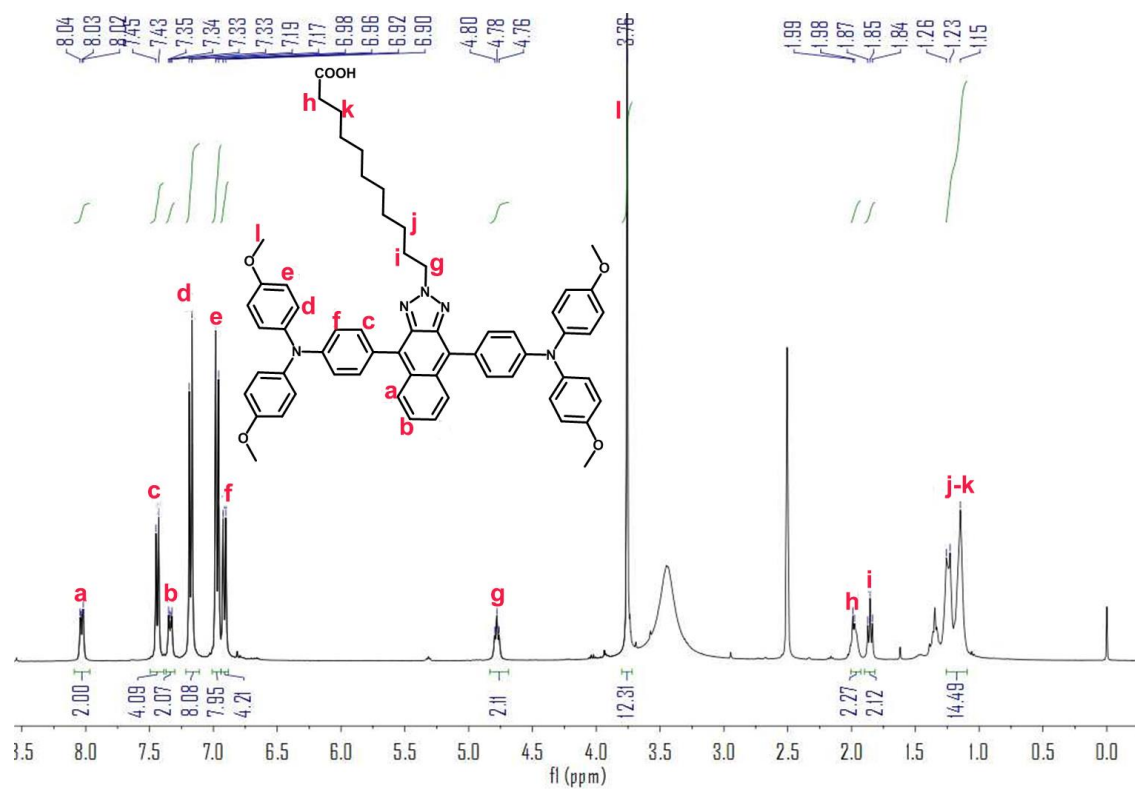

Figure S2. ¹³C NMR of Intermediate **5**

31

Figure S3. ^{1}H NMR of Compound **1**
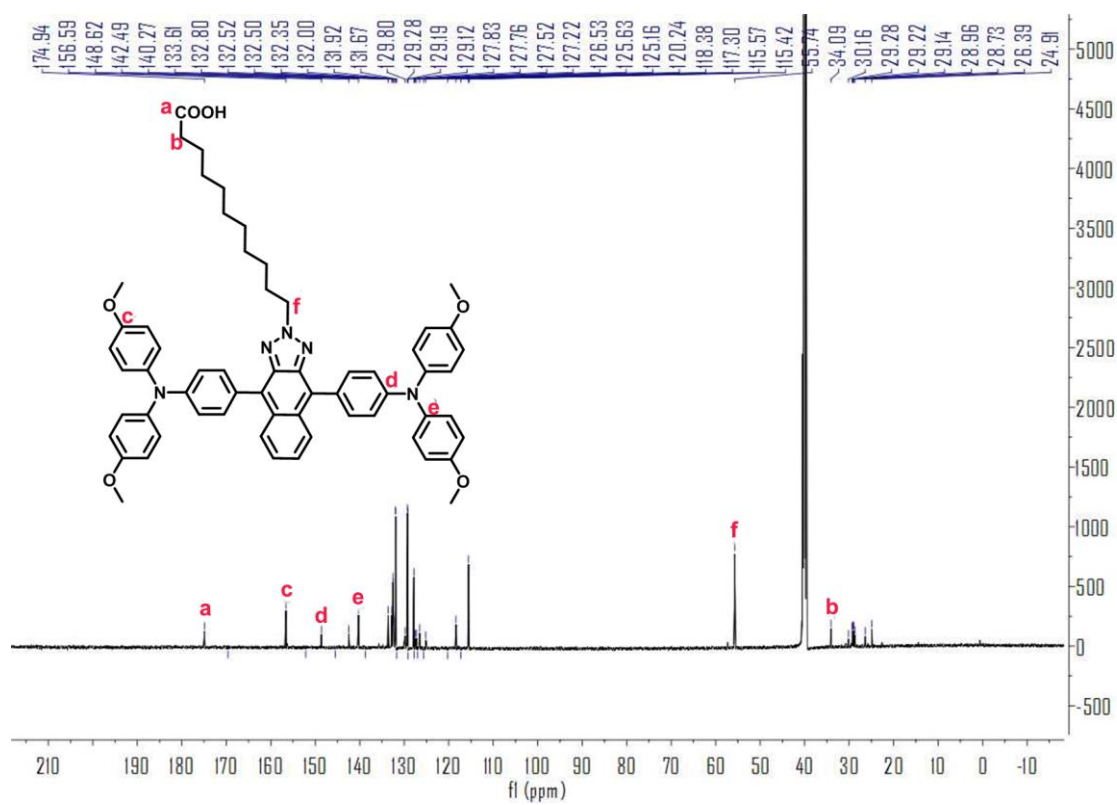
Figure S4. ^{13}C NMR of Compound **1**
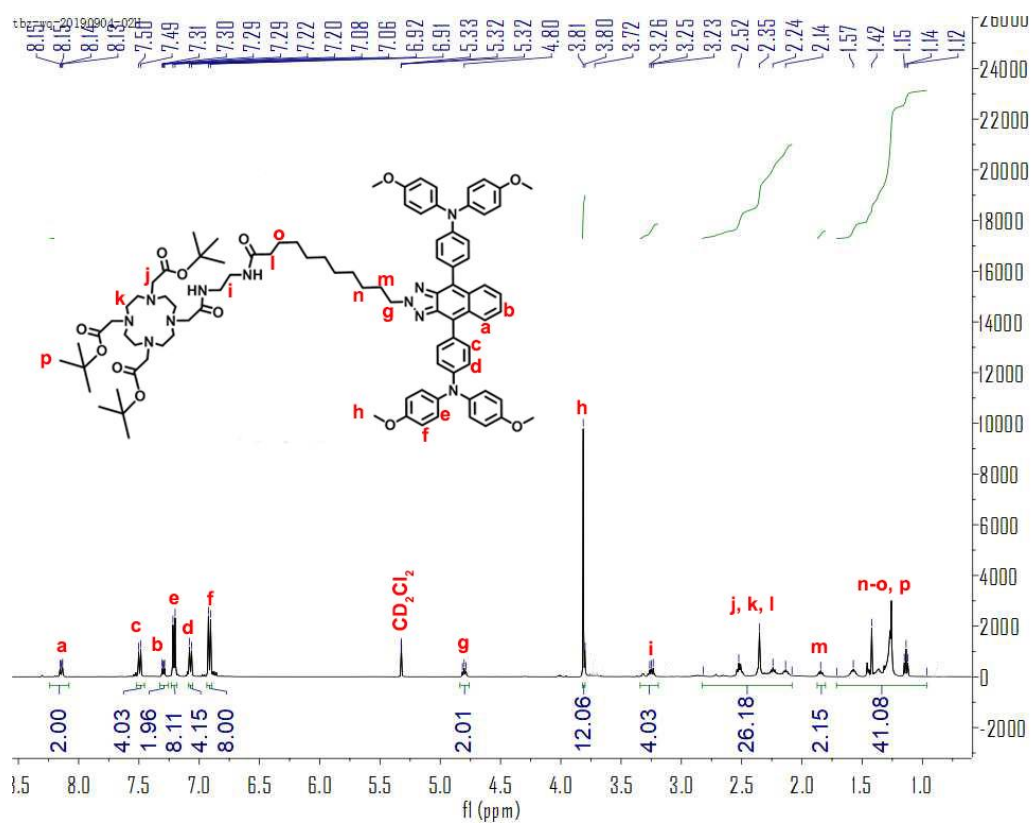
Figure S5. ^{1}H NMR of Compound 3 (N-DO3A*t*Bu)
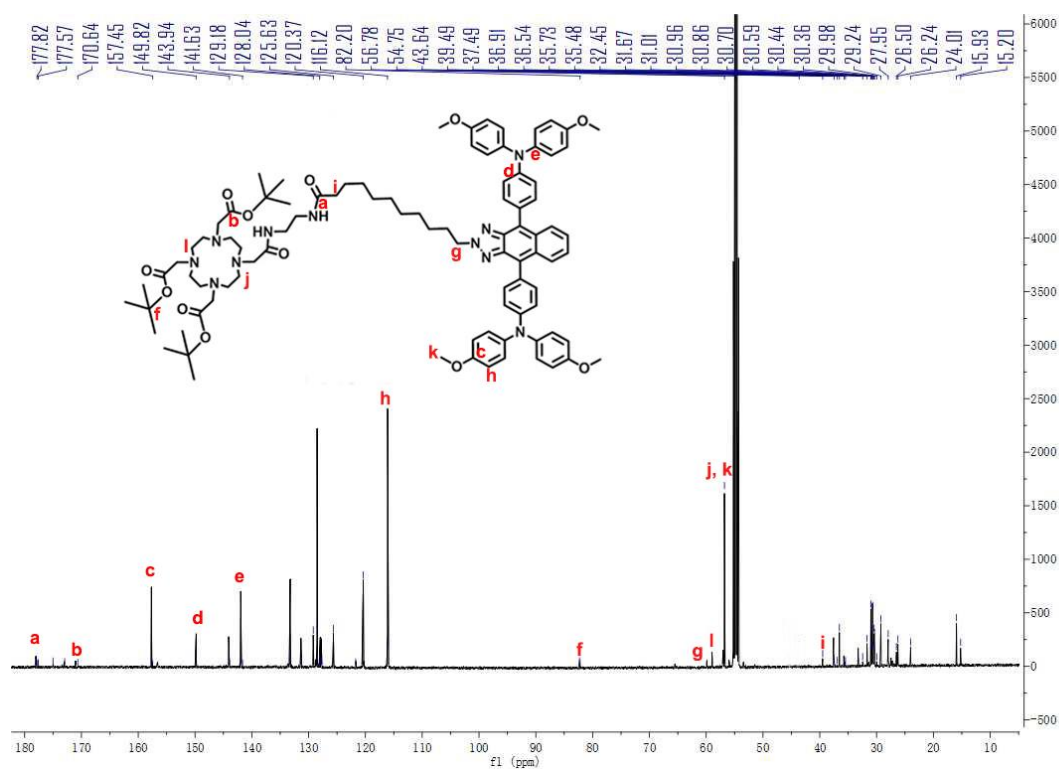
Figure S6. ^{13}C NMR of Compound 3 (N-DO3A*t*Bu)
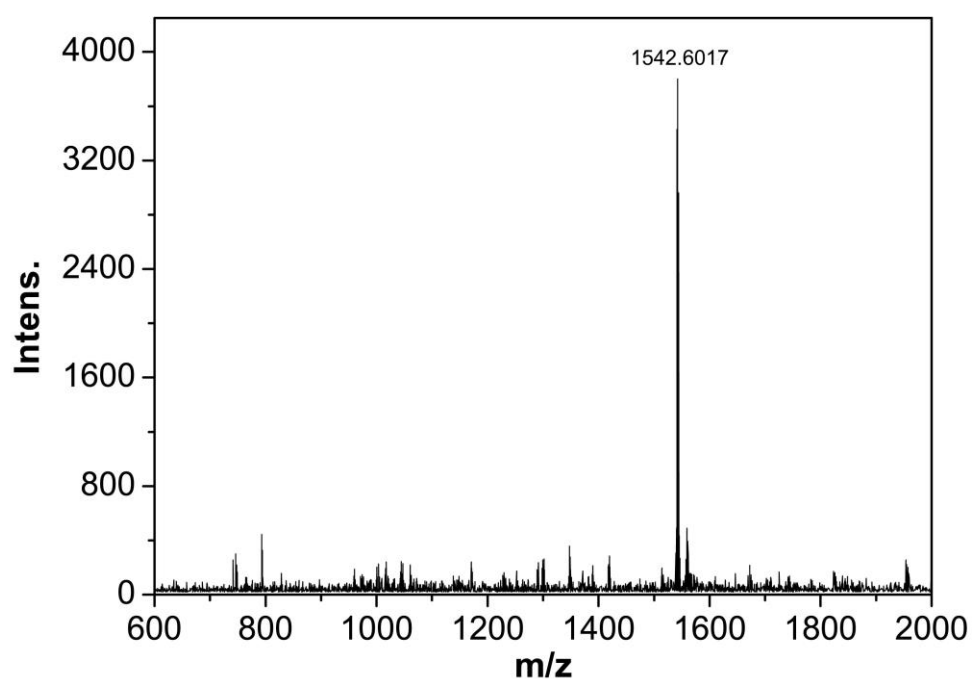
Figure S7. HR-MS of NGd
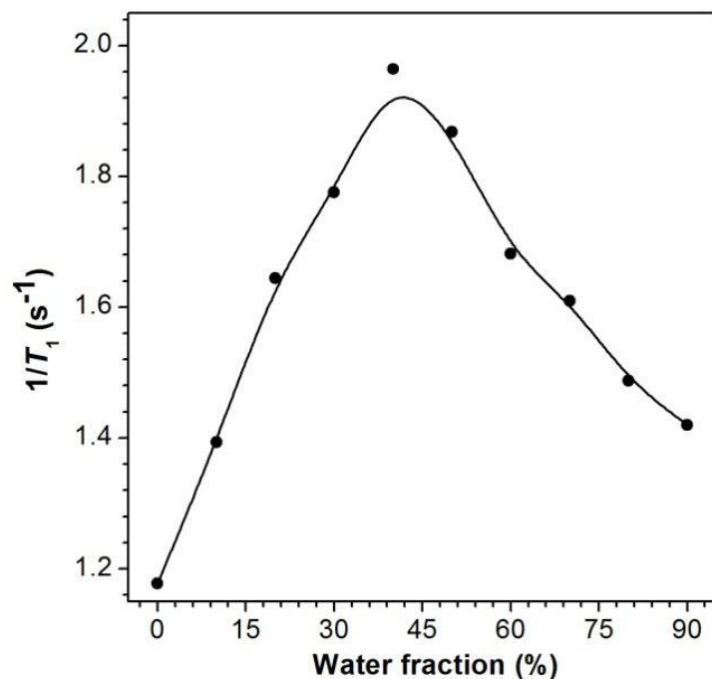
Figure S8. The relaxivities of NGd (0.1 mM [Gd]) in mixtures of DMSO/water with different water fraction (f_w).
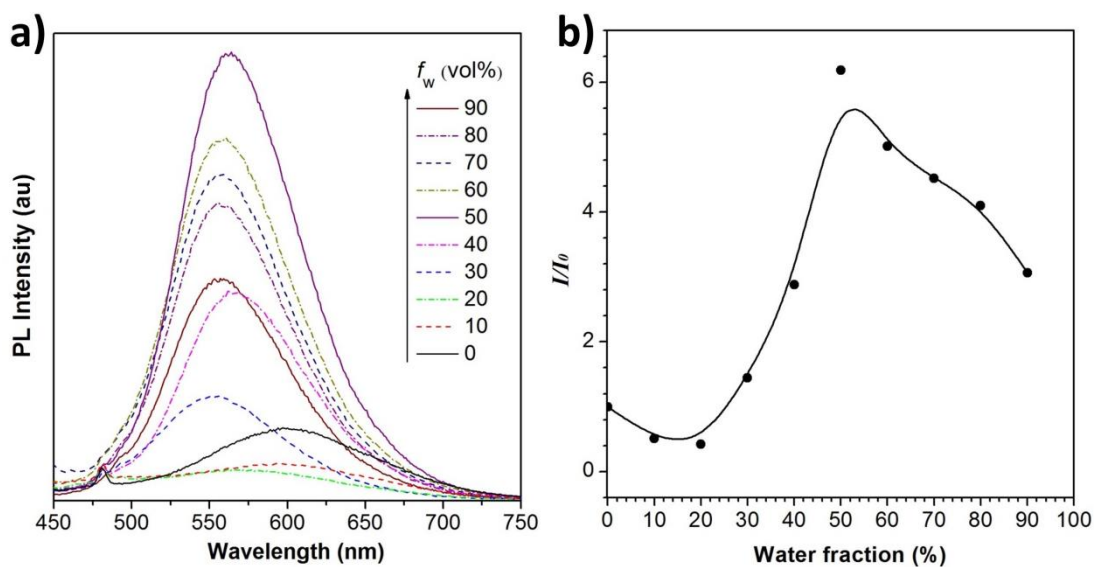

Figure S9. (a) Photoluminescence (PL) spectra of N-DO3A*t*Bu (10 μM) in mixtures of DMSO/water with different water fraction (f_w). (b) Plots of the relative emission intensity of N-DO3A*t*Bu versus water fraction. I_0 and I are the peak values of PL intensities of N-DO3A*t*Bu (10 μM) in DMSO and DMSO/water mixtures, respectively.
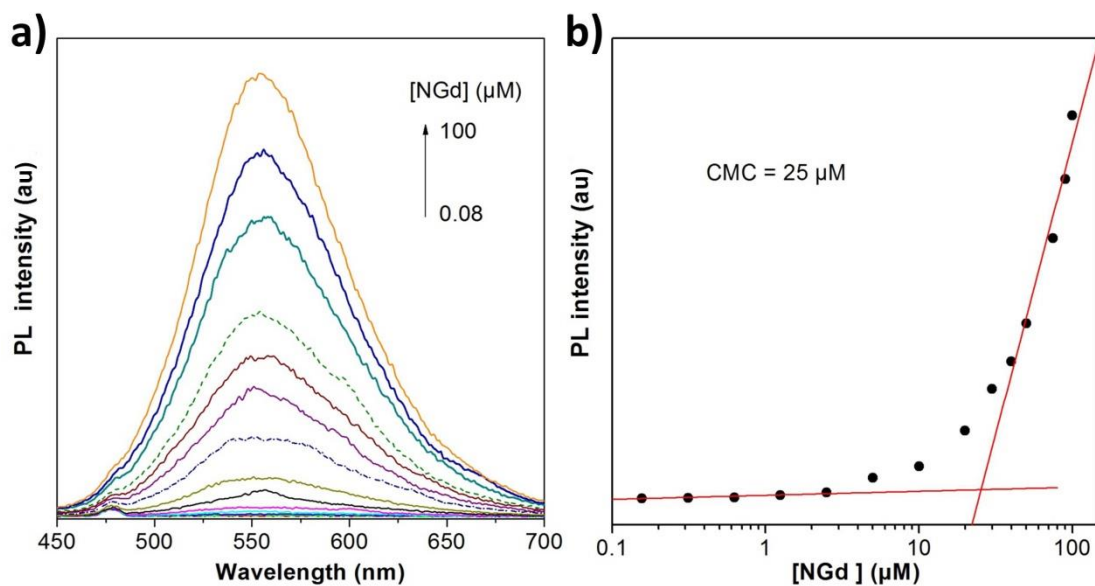
Figure S10. Critical micelle concentration (CMC) of NGd. Plotting the fluorescence intensity (a) versus the dye concentration generates two lines (b), the intersection of which gives the CMC of 25 μM.
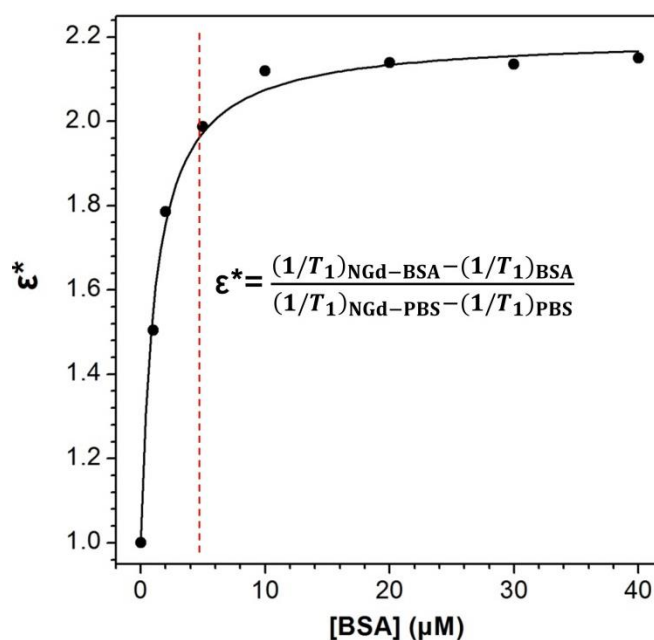

$$\varepsilon^* = \frac{(1/T_1)_{NGd-BSA} - (1/T_1)_{BSA}}{(1/T_1)_{NGd-PBS} - (1/T_1)_{PBS}}$$

Figure S11. Relaxation enhancement curve of NGd with the increase of BSA concentration. ε^* is the enhanced factor, and the concentration of NGd is 10 μM. The red dotted line is the mark of the molar ratio of BSA/NGd of 1:2, which is as the initial feed ratio to synthesize the NGd-ACs.
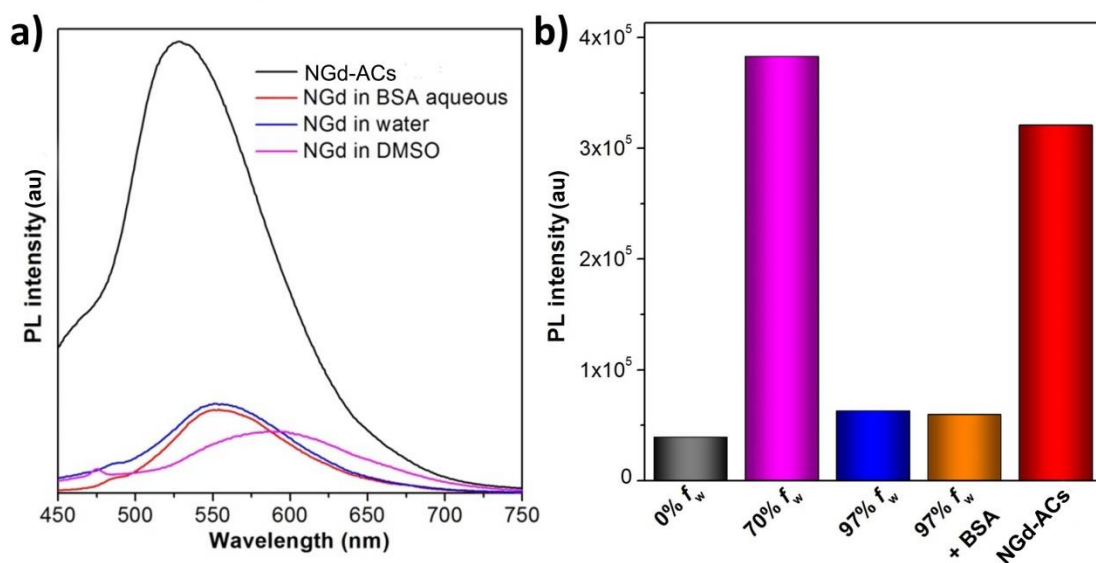
Figure S12. (a) Photoluminescence intensity of NGd-ACs, NGd molecules in DMSO, water, BSA aqueous solution (the molar ratio of NGd/BSA = 2:1), respectively. (b) Comparison of photoluminescence (PL) intensity of NGd (10 μM) in mixtures of water/DMSO with 0, 70%, 97%, 97% (BSA) water fraction (f_w), respectively, and NGd-ACs (10 μM).

Table S1. Maximum emission, PL intensity and quantum yield (Φ_F) of NGd-ACs, and NGd in different solvents (BSA aqueous, Deionized water, and DMSO), respectively.

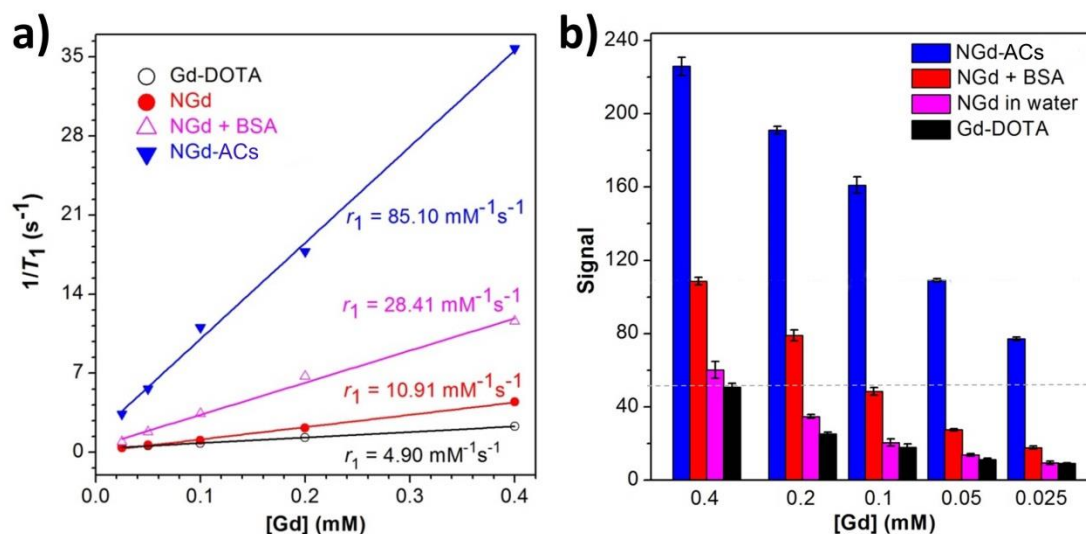|	λ_{em} [nm]	Φ_F [%]
NGd-ACs	529	14.2± 0.1
NGd in BSA aqueous	552	2.4±0.2
NGd in water	551	2.0±0.2
NGd in DMSO	594	4.1±0.1

Figure S13. (a) T_1 relaxivities of NGd-ACs, NGd in BSA aqueous solution (the molar ratio of NGd/BSA = 2:1), NGd in water, and Gd-DOTA at 0.5 T, respectively. (b) The signals of phantom images of NGd-ACs, NGd in BSA aqueous, NGd in water, and Gd-DOTA at different Gd(III) concentrations measured by ImageJ, respectively.
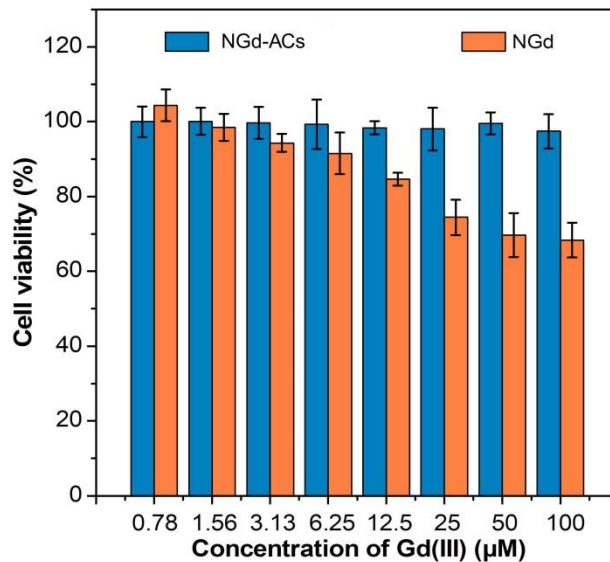

Figure S14. Cell viability of NGd-ACs and NGd by MTT.

Reference

[1] P. Wei, L. Duan, D. Zhang, J. Qiao, L. Wang, R. Wang, G. Dong, Y. Qiu, *J. Mater. Chem.* **2008**, *18*, 806.

[2] Y.-S. Yen, J.-S. Ni, W.-I. Hung, C.-Y. Hsu, H.-H. Chou, J.-T. s. Lin, *ACS Appl. Mater. Inter.* **2016**, *8*, 6117.

[3] a) L. Wang, H. Lin, L. Ma, J. Jin, T. Shen, R. Wei, X. Wang, H. Ai, Z. Chen, J. Gao, *Nanoscale* **2017**, *9*, 4516; b) L. Wang, H. Lin, L. Ma, C. Sun, J. Huang, A. Li, T. Zhao, Z. Chen, J. Gao, *J. Mater. Chem. B* **2017**, *5*, 8004.

[4] A. C. Esqueda, J. A. Lopez, G. Andreu-de-Riquer, J. C. Alvarado-Monzon, J. Ratnakar, A. J. Lubag, A. D. Sherry, L. M. De Leon-Rodriguez, *J. Am. Chem. Soc.* **2009**, *131*, 11387.

[5] J. Y. Jun, H. H. Nguyen, S.-Y.-R. Paik, H. S. Chun, B.-C. Kang, S. Ko, *Food Chemistry* **2011**, *127*, 1892.